

## Research papers

# Electrospun carbon nanofibers embedded with heterostructured NiFe<sub>2</sub>O<sub>4</sub>/Fe<sub>0.64</sub>Ni<sub>0.36</sub> nanoparticles as an anode for high-performance lithium-ion battery

Shujin Hao<sup>a,1</sup>, Xiaoli Sheng<sup>a,1</sup>, Fei Xie<sup>a</sup>, Meng Sun<sup>a</sup>, Feiyu Diao<sup>b,\*</sup>, Yiqian Wang<sup>a,\*</sup>

<sup>a</sup> College of Physics, Qingdao University, No. 308 Ningxia Road, Qingdao 266071, PR China

<sup>b</sup> Industrial Research Institute of Nonwovens & Technical Textiles, Shandong Center for Engineered Nonwovens, College of Textiles & Clothing, Qingdao University, No. 308 Ningxia Road, Qingdao 266017, PR China



## ARTICLE INFO

## Keywords:

Lithium-ion batteries  
Carbon nanofibers  
Heterostructure  
Ni-Fe based nanoparticles  
Electrospinning

## ABSTRACT

Binary transition metal compounds exhibit promising application potential as anode materials in the field of lithium-ion batteries (LIBs) due to their high theoretical specific capacity. However, their poor electrical conductivity and drastic volume expansion during charge and discharge processes limit their high-performance applications. Herein, we have synthesized carbon nanofibers (CNFs) loaded with heterostructured Ni–Fe based nanoparticles (NiFe<sub>2</sub>O<sub>4</sub>/Fe<sub>0.64</sub>Ni<sub>0.36</sub>@CNFs) using electrospinning, and explore their cyclic stability and rate performances. By subjecting the electrospun membranes to thermal treatment at different annealing temperatures, three distinct phases of Ni–Fe compounds embedded in CNFs, *i.e.*, NiFe<sub>2</sub>O<sub>4</sub> (400 °C), NiFe<sub>2</sub>O<sub>4</sub>/Fe<sub>0.64</sub>Ni<sub>0.36</sub> (500 °C) and Fe<sub>0.64</sub>Ni<sub>0.36</sub> (800 °C), are obtained. When they are used as anode materials, the electrochemical properties are investigated. The NiFe<sub>2</sub>O<sub>4</sub>/Fe<sub>0.64</sub>Ni<sub>0.36</sub>@CNFs anode material exhibits the best cycling and rate performances, with a capacity of 431.1 mAh g<sup>-1</sup> achieved after 200 cycles at a current density of 0.2 A g<sup>-1</sup>. Moreover, its specific capacities are 558.9, 400.1, 272.4, 178.1 and 89.5 mAh g<sup>-1</sup> at current densities of 0.1, 0.2, 0.5, 1.0 and 2.0 A g<sup>-1</sup>, respectively. As the current density returns to 0.1 A g<sup>-1</sup>, its specific discharge capacity can reach 527.5 mAh g<sup>-1</sup>. The excellent cycling and rate performances of NiFe<sub>2</sub>O<sub>4</sub>/Fe<sub>0.64</sub>Ni<sub>0.36</sub>@CNFs are mainly attributed to the following reasons: i) the carbon fibers can effectively alleviate volume expansion and structural stress during cycling; ii) Fe<sub>0.64</sub>Ni<sub>0.36</sub> alloy can inhibit the formation of lithium dendrites and effectively reduce the nucleation overpotential of metallic lithium, thereby improving the electrochemical stability; iii) the heterostructure can improve electrochemical properties through the synergistic interaction between NiFe<sub>2</sub>O<sub>4</sub> and Fe<sub>0.64</sub>Ni<sub>0.36</sub>. The catalytic Fe<sub>0.64</sub>Ni<sub>0.36</sub> not only facilitate the conversion reaction of NiFe<sub>2</sub>O<sub>4</sub>, resulting in the high capacity, but also increase the conductivity of the material. This work offers a feasible strategy to significantly improve the electrochemical performance of binary metal compounds, paving the way for their practical applications in the high-performance LIBs.

## 1. Introduction

Recently, Ni–Fe based metal compounds have drawn extensive scientific interest as anode materials in lithium-ion batteries (LIBs) owing to their elevated theoretical specific capacity and corrosion resistance [1–3]. However, their applications are inevitably constrained by poor electronic conductivity and severe volume changes during the charge and discharge processes [4,5]. Therefore, it becomes imperative to overcome these problems using different strategies.

Many researchers have devoted great efforts to the improvement of the electrochemical performance of Ni–Fe based metal compounds. As a common strategy, carbon coating has been used to enhance the cycling stability of Ni–Fe based nanostructures as anode materials, which can alleviate the volume change during the charge/discharge process [6,7]. For example, Yang *et al.* [8] produced NiFe<sub>2</sub>O<sub>4</sub> nanoparticles embedded in carbon nanofibers (CNFs) by electrospinning, which exhibited excellent cycling stability with a discharge capacity of 497.1 mAh g<sup>-1</sup> after 100 cycles at 0.1 A g<sup>-1</sup>, and indicated that the CNFs

\* Corresponding authors.

E-mail addresses: [fydiao@qdu.edu.cn](mailto:fydiao@qdu.edu.cn) (F. Diao), [yqwang@qdu.edu.cn](mailto:yqwang@qdu.edu.cn) (Y. Wang).

<sup>1</sup> Shujin Hao and Xiaoli Sheng contributed equally to this work.

can shorten the diffusion path of  $\text{Li}^+$  ions and restrain the particles pulverization/agglomeration during cycling. Liu et al. [9] loaded FeNi nanoparticles on CNFs by electrospinning and further demonstrated that the carbon fibers significantly improved the cycling and rate performances of anode materials. However, the introduction of carbon material results in the reduction of specific capacity for anode due to its relatively low theoretical specific capacity ( $372 \text{ mAh g}^{-1}$ ) [10]. To solve this problem, researchers have made much endeavor to develop other strategies, *i.e.*, constructing heterostructures, to increase the specific capacity of Ni–Fe based metal compounds [11,12]. For example, Wang et al. [13] prepared NiO/NiFe<sub>2</sub>O<sub>4</sub> heterostructure as an anode for LIBs and revealed that the hetero-interfaces facilitated rapid charge transport. In this context, designing anodes using heterostructured Ni–Fe based nanoparticles embedded in CNFs is expected to achieve excellent cycling stability and high specific capacity, which is proven to be a more feasible strategy to enhance the electrochemical performance.

In this work, Ni–Fe based nanoparticles embedded in CNFs are prepared through electrospinning and subsequent annealing processes. Three distinct Ni–Fe based nanostructures embedded in CNFs are obtained at different annealing temperatures, *i.e.*, NiFe<sub>2</sub>O<sub>4</sub>@CNFs (400 °C), Fe<sub>0.64</sub>Ni<sub>0.36</sub>/NiFe<sub>2</sub>O<sub>4</sub>@CNFs (500 °C), and Fe<sub>0.64</sub>Ni<sub>0.36</sub>@CNFs (800 °C), and their electrochemical performances are explored. All the anode materials show an excellent cycling performance due to the mitigation effect of CNFs on volume expansion. Furthermore, among the three anode materials, NiFe<sub>2</sub>O<sub>4</sub>/Fe<sub>0.64</sub>Ni<sub>0.36</sub>@CNFs exhibits the best electrochemical performance due to the synergistic interaction of NiFe<sub>2</sub>O<sub>4</sub>/Fe<sub>0.64</sub>Ni<sub>0.36</sub>.

## 2. Experimental

### 2.1. Materials

The carbon source in the samples is provided by the polyacrylonitrile (PAN, average Mw 150,000), while Fe and Ni sources are obtained from iron acetylacetonate [Fe(acac)<sub>3</sub>, 98 %] and nickel acetylacetonate [Ni(acac)<sub>2</sub>, 95 %]. The solvent is *N,N*-dimethylformamide (DMF, 99.5 %) supplied by Sinopharm Chemical Reagent Co., Ltd. All the chemicals have not undergone further purification.

### 2.2. Synthesis of Ni–Fe based nanoparticles embedded in CNFs

First, a viscous solution was prepared by dissolving PAN(11 wt%), DMF, Fe(acac)<sub>3</sub> and Ni(acac)<sub>2</sub> (a molar ratio of 2:1). Subsequently, the solution was spun into a fiber membrane by electrospinning under specific conditions: the relative humidity is 33 %–36 %; the temperature is 25 °C. The injection rate and applied voltage were set as 0.36 mL/h and 20 kV, the roll speed was 500–600 rpm, and the distance between the receiver surface and needle (a internal diameter of 0.55 mm) was 16 cm. The fiber membranes were produced after electrospinning for 8 h, then dried at room temperature for 2 h to remove residual solvents. Afterwards, pre-oxidation treatment was conducted on the fiber membrane for 2 h at 230 °C in air. Finally, an annealing process was carried out at different temperatures (400 °C, 500 °C and 800 °C) with a heating rate of 2 °C/min in an argon atmosphere to form Ni–Fe based nanoparticles embedded in CNFs. We labeled the resulting membranes as NF-P 400, NF-P 500 NF-P 800 and P-800, respectively.

### 2.3. Materials characterization

The morphology of the resultant membranes was examined using field-emission scanning electron microscopy (FE-SEM, Sigma 500) operated at 20 kV and transmission electron microscope (TEM JEOL JEM 2100F) operated at 200 kV. The elemental mapping of the nanofibers was tested by energy dispersive X-ray spectrometer (EDS, Oxford INCAx-Sight6427). The phase composition of the fiber membranes was analyzed using an X-ray diffractometer (XRD, Bruker D8 Advance) with

Cu-K $\alpha$  radiation ( $\lambda = 1.5406 \text{ \AA}$ ). Thermogravimetric analysis (TGA, Germany NETZSCH TG209F3) was carried out to investigate the phase transformation process. The elemental composition was tested by X-ray photoelectron spectroscopy (XPS, Thermo Scientific K-Alpha<sup>+</sup>).

### 2.4. Measurement of electrochemical properties

The flexible membranes were directly utilized as binder-free working electrode. Simultaneously, we determined the weight of each electrode as the mass of the active substance. A mixed solution consisting of 1 M LiPF<sub>6</sub> and ethylene carbonate (EC)/diethyl carbonate (DEC)/dimethyl carbonate (DMC) (1:1:1 in volume) was employed as the electrolyte, and lithium foil served as a counter electrode. The CR2025 button battery was assembled in a high-purity argon-filled glove box, maintaining moisture and oxygen levels below 0.1 ppm. The cycling and rate performances were investigated using the LAND testing system (voltage range: 0.01 V to 3.00 V). Cyclic voltammetry (CV) analysis was conducted using a Metrohm Autolab electrochemical workstation. Electrochemical impedance spectroscopy (EIS) measurements were performed on a Metrohm Autolab electrochemical workstation under open circuit voltage conditions (frequency range from 100 kHz to 0.01 Hz, interference amplitude of 5 mV).

## 3. Results and discussion

### 3.1. Morphology and microstructure of fiber membranes

To explore the morphologies of fiber membranes obtained at different temperatures, NF-P 400, NF-P 500 and NF-P 800 are characterized by SEM. The SEM images in Fig. 1a, d and g indicate that the fibers have uniform diameters, smooth surface without beads. In addition, as the annealing temperature increases, the diameter of the fibers gradually decreases, because more gas is produced and released from the fibers. To get further insight about the morphology and phase transformations, TEM examinations are conducted on the same membranes. The bright-field TEM image of NF-P 400 (Fig. 1b) reveals the presence of many small nanoparticles loaded onto the submicron carbon fibers. In Fig. 1c, the lattice plane spacings in the crystalline region of these nanoparticles are measured to be 2.9 Å and 2.5 Å, which correspond to the (220) and ( $\bar{3}$ 31) crystal planes of cubic NiFe<sub>2</sub>O<sub>4</sub>, respectively. Furthermore, the measured angle between the crystal planes is found to be 66°, consistent with the theoretical values for cubic NiFe<sub>2</sub>O<sub>4</sub>. In Fig. 1f, the measured lattice spacings of region I are 2.9 Å and 2.1 Å, corresponding to the (022) and (400) crystal planes of NiFe<sub>2</sub>O<sub>4</sub>, respectively. In addition, the measured angle between these two crystal planes is 90°, which is expected for a cubic lattice. Moreover, in region II, the measured lattice spacing is 2.0 Å, consistent with the (111) crystal plane of Fe<sub>0.64</sub>Ni<sub>0.36</sub>. From the above analysis, it can be concluded that the NF-P 500 consists of NiFe<sub>2</sub>O<sub>4</sub> and Fe<sub>0.64</sub>Ni<sub>0.36</sub> with a hetero-interface between the two phases. The interplanar spacing in Fig. 1i is measured to be 1.8 Å, corresponding to the {200} crystal planes of Fe<sub>0.64</sub>Ni<sub>0.36</sub>.

The elemental distributions of NF-P 400, NF-P 500, and NF-P 800 were examined through EDS elemental mappings, as depicted in Fig. 2. To explore its composition more detailly, the atomic ratios of various elements (C, O, Fe and Ni) and the contents of different components (C, NiFe<sub>2</sub>O<sub>4</sub> and Fe<sub>0.64</sub>Ni<sub>0.36</sub>) were presented in Tables S1 and S2, respectively, consistent with the data we previously tested. To further investigate the phase transformation of Ni–Fe based compounds within carbon fibers, TGA measurements of NF-P and pure PAN (P) fibers were conducted in Fig. S1. Firstly, the temperature increases processes is divided into two parts, including the temperature from 30 °C up to 230 °C in air atmosphere and the temperature from 230 °C up to 850 °C in Ar atmosphere with a heating rate of 10 °C/min. The formation of NiFe<sub>2</sub>O<sub>4</sub> could be observed from 352 to 485 °C. With the temperature increasing, the temperature-dependent transformation from NiFe<sub>2</sub>O<sub>4</sub> to

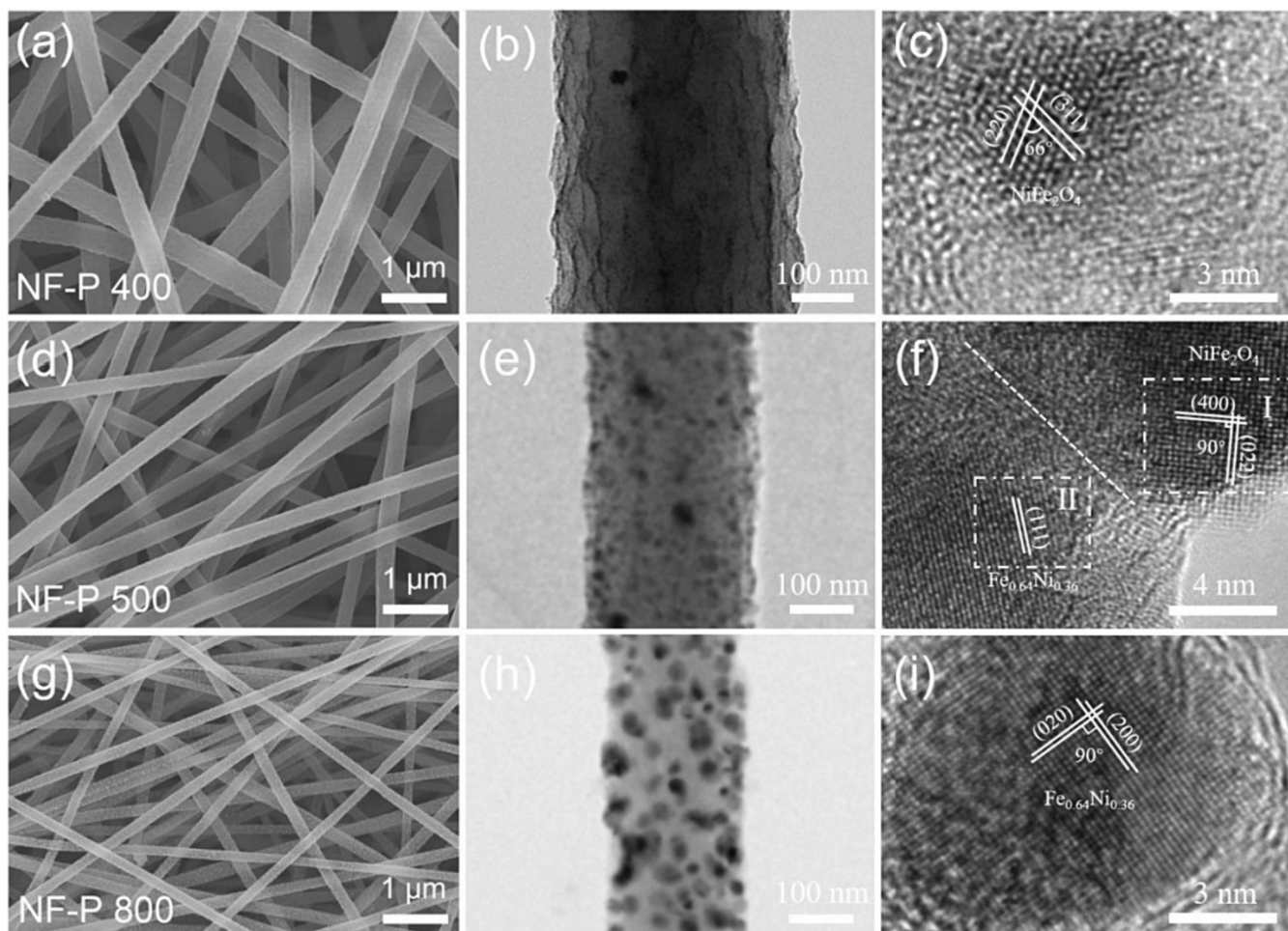


Fig. 1. SEM and TEM images of NF-P 400 (a, b and c), NF-P 500 (d, e and f) and NF-P 800 (g, h and i).

$\text{Fe}_{0.64}\text{Ni}_{0.36}$  was observed at 485 up to 762 °C. When the temperature reaches up to 762 °C until 850 °C, the curve of NF-P membrane is parallel to that of PAN (P), which means the transformation is already completed at 762 °C. So, it is reasonable to deduce that the transformation from  $\text{NiFe}_2\text{O}_4$  to  $\text{Fe}_{0.64}\text{Ni}_{0.36}$  is completed at 800 °C. Furthermore, Raman spectroscopy analysis in our previous work [14] showed that the graphitization degree of the samples increased with an increase in annealing temperature and NF-P-800 exhibited the highest degree of graphitization.

With  $\text{Cu-K}\alpha$  radiation ( $\lambda = 1.5406 \text{ \AA}$ ), XRD is employed to identify the structure of the NF-P membranes obtained at different annealing temperatures, as displayed in Fig. 3. The diffraction peaks become gradually sharp with increasing annealing temperatures, because elevating temperature can improve the crystallinity of the product. This is corroborated by TEM images from which it can be seen that the nanoparticles are much larger in NF-P 800 (Fig. 1h) than those in NF-P 400 and NF-P 500 (Fig. 1b and e). The XRD pattern of NF-P 400 (Fig. 3a) indicates that a diffusive broad peak at  $\sim 26^\circ$  stands for the diffraction peak from amorphous carbon, and the peaks at  $30.3^\circ$ ,  $35.7^\circ$  and  $62.9^\circ$  correspond to the crystal planes of (220), (331) and (440) of cubic  $\text{NiFe}_2\text{O}_4$  (JCPDS no.: 10-0325,  $a = 8.339 \text{ \AA}$ ), respectively [15], which indicates that  $\text{NiFe}_2\text{O}_4$  nanocrystals start to form in submicron carbon fibers at 400 °C. Fig. 3b is the XRD pattern of NF-P 500, in which the peak at  $43.6^\circ$  is caused by the overlapped diffraction from both (111) plane of cubic  $\text{Fe}_{0.64}\text{Ni}_{0.36}$  (JCPDS no.: 47-1405,  $a = 3.5922 \text{ \AA}$ ) and (400) plane of cubic  $\text{NiFe}_2\text{O}_4$  [16]. The diffraction peak at  $50.8^\circ$  corresponds to the (200) crystal plane of the cubic  $\text{Fe}_{0.64}\text{Ni}_{0.36}$ , suggesting that some  $\text{NiFe}_2\text{O}_4$  has been reduced to  $\text{Fe}_{0.64}\text{Ni}_{0.36}$  by carbon in the

CNFs at 500 °C. Quantitative analysis of the XRD pattern for NF-P 500 shows that the mass ratio of  $\text{NiFe}_2\text{O}_4$  to  $\text{Fe}_{0.64}\text{Ni}_{0.36}$  in NF-P 500 is approximately 1:3.5. Meanwhile, in the XRD pattern of NF-P 800 (Fig. 3c), three diffraction peaks at  $43.6^\circ$ ,  $50.8^\circ$  and  $74.7^\circ$  correspond to the (111), (200) and (220) crystal planes of the cubic  $\text{Fe}_{0.64}\text{Ni}_{0.36}$ , which indicates that  $\text{NiFe}_2\text{O}_4$  has been completely reduced into  $\text{Fe}_{0.64}\text{Ni}_{0.36}$  by carbon in the CNFs at 800 °C. From the above analysis, the  $\text{NiFe}_2\text{O}_4$  is produced in the submicron carbon fibers at 400 °C. At 500 °C, metallic oxide  $\text{NiFe}_2\text{O}_4$  and intermetallic compound  $\text{Fe}_{0.64}\text{Ni}_{0.36}$  co-exist in CNFs, and the intermetallic compound  $\text{Fe}_{0.64}\text{Ni}_{0.36}$  forms in the CNFs at 800 °C, which indicates that the phase transformation process has been completed at 800 °C. Therefore, the phase and composition of the product can be adjusted by changing the annealing temperature.

To gain further insight into the valence states of Ni and Fe in  $\text{NiFe}_2\text{O}_4$  and  $\text{Fe}_{0.64}\text{Ni}_{0.36}$  embedded in the CNFs, we characterize NF-P 400 and NF-P 800 using XPS. Fig. 3d and g show the full XPS spectrum of NF-P 400 and NF-P 800, respectively. Fig. 3e and f present the spectra of Ni 2p and Fe 2p in NF-P 400, where two peaks at 873 eV and 855 eV are attributed to Ni 2p<sub>1/2</sub> and Ni 2p<sub>3/2</sub> of  $\text{Ni}^{2+}$ . Additionally, two peaks are observed at 724 eV and 710 eV, corresponding to Fe 2p<sub>1/2</sub> and Fe 2p<sub>3/2</sub> of  $\text{Fe}^{3+}$ , respectively [17]. Based on the above analysis, the valence states of Ni and Fe elements present in NF-P 400 are determined to be  $\text{Ni}^{2+}$  and  $\text{Fe}^{3+}$ , respectively. Specifically, the peaks observed in the Ni 2p spectra (Fig. 3h) of NF-P 800 indicate that the binding energy values are 871 eV and 853 eV, corresponding to Ni 2p<sub>1/2</sub> and Ni 2p<sub>3/2</sub> of  $\text{Ni}^0$ , respectively. The XPS spectrum of Fe 2p in NF-P 800 (Fig. 3i) displays two peaks, which can be ascribed to the Fe 2p<sub>1/2</sub> (721 eV) and Fe 2p<sub>3/2</sub> (707 eV) of  $\text{Fe}^0$  [18,19]. Based on the aforementioned analysis, it can be

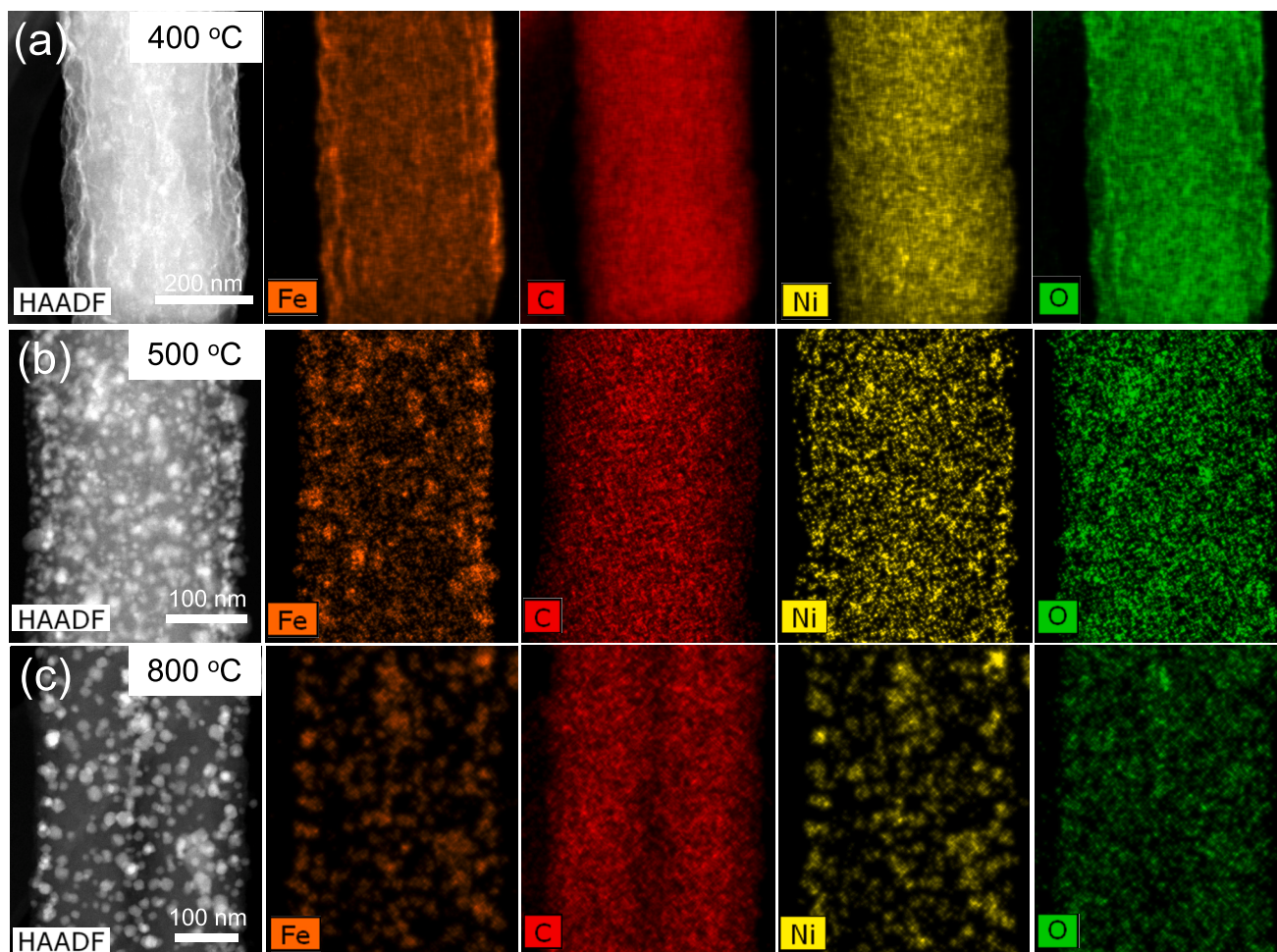


Fig. 2. HAADF-STEM images and EDS elemental mappings of (a) NF-P 400, (b) NF-P 500 and (c) NF-P 800.

concluded that the valence states of Ni and Fe elements in NF-P 800 are  $\text{Ni}^0$  and  $\text{Fe}^0$ , confirming the complete reduction of the  $\text{NiFe}_2\text{O}_4$ .

### 3.2. Electrochemical performances of fiber membranes

NF-P 400, NF-P 500 and NF-P 800 are investigated as anode materials for LIBs to examine their electrochemical performances. Fig. 4a shows the CV curves of the third cycle for NF-P 400, NF-P 500, and NF-P 800 electrodes at a scan rate of  $0.1 \text{ mV s}^{-1}$  (voltage range 0.01–3.00 V). During cathodic process, the peak at 0.80 V corresponds to the reduction of  $\text{Ni}^{2+}$  and  $\text{Fe}^{3+}$  to  $\text{Ni}^0$  and  $\text{Fe}^0$  [20]. The conversion reaction [5] of the  $\text{NiFe}_2\text{O}_4$  involves the insertion of  $\text{Li}^+$ , and the equation for the electrochemical reaction is displayed as follows [21].

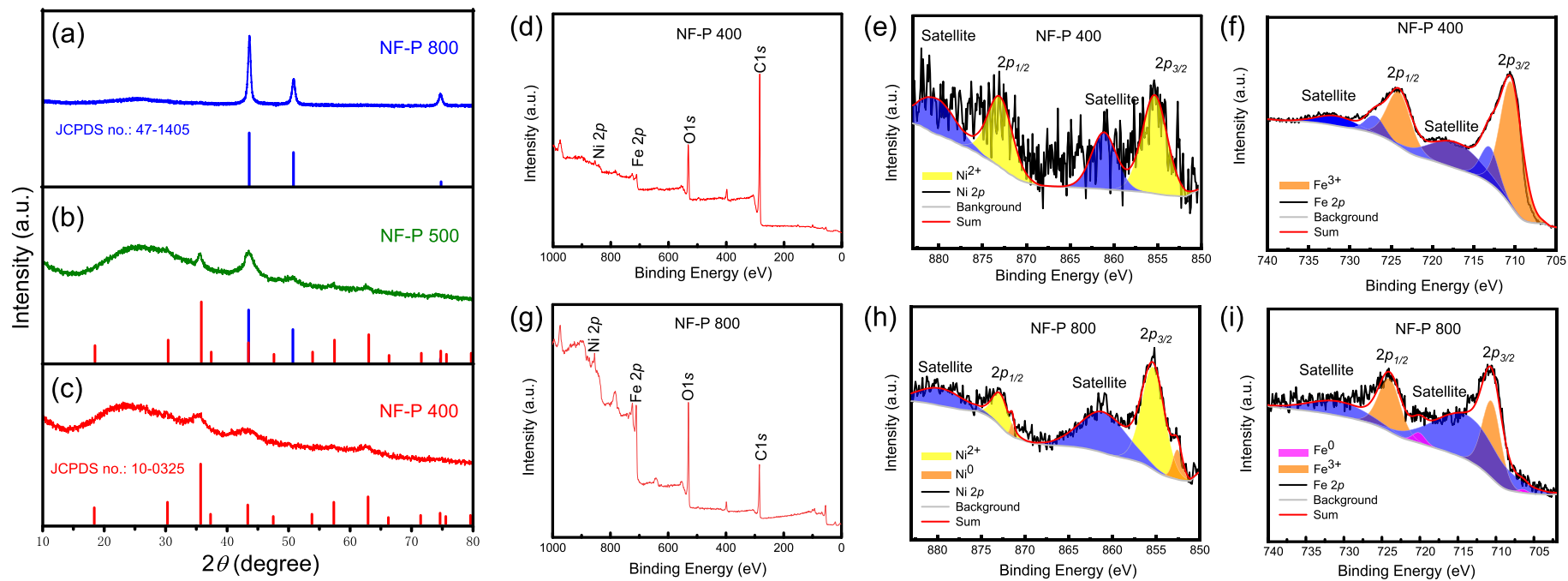


During anodic process, the peak at 1.25 V corresponds to the oxidation of  $\text{Fe}^0$  and  $\text{Ni}^0$  into  $\text{Fe}^{3+}$  and  $\text{Ni}^{2+}$ . The electrochemical reactions are shown in Equ. (2) and (3) as follows [22].

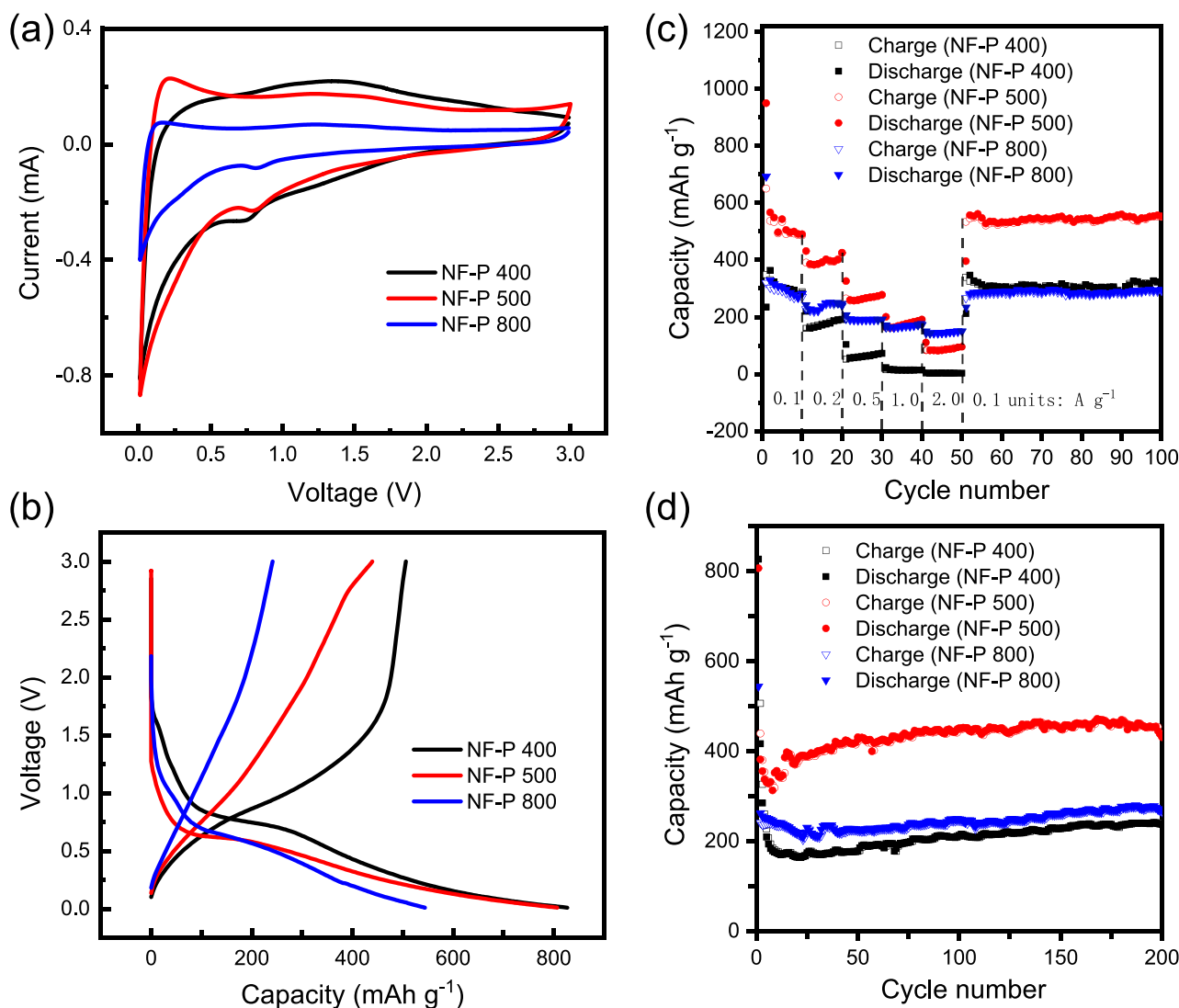


Fig. 4b shows the initial charge-discharge curves of NF-P 400, NF-P 500, and NF-P 800 electrodes at a current density of  $0.2 \text{ A g}^{-1}$ . The initial specific discharge capacities of NF-P 400, NF-P 500, and NF-P 800 electrodes are 826, 806, and  $543 \text{ mAh g}^{-1}$ , respectively. It can be seen that the initial specific discharge capacity of the electrodes decreases as the annealing temperature increases. This is attributed to the fact that

$\text{NiFe}_2\text{O}_4$  possesses a high theoretical specific capacity ( $915 \text{ mAh g}^{-1}$ ) [23] and more  $\text{NiFe}_2\text{O}_4$  converts into  $\text{Fe}_{0.64}\text{Ni}_{0.36}$  as the annealing temperature increases. Fig. 4c demonstrates the rate performance of NF-P 400, NF-P 500 and NF-P 800 electrodes. For the NF-P 500 electrodes, the average specific discharge capacities are 558.9, 400.1, 272.4, 178.1 and  $89.5 \text{ mAh g}^{-1}$  at current densities of 0.1, 0.2, 0.5, 1.0 and  $2.0 \text{ A g}^{-1}$ , respectively. When the current density returns to  $0.1 \text{ A g}^{-1}$ , the specific discharge capacity of NF-P 500 electrode reaches  $527.5 \text{ mAh g}^{-1}$ , indicating that NF-P 500 electrode has an excellent rate performance. Fig. 4d shows the cycling performance of the NF-P 400, NF-P 500, and NF-P 800 electrodes at a current density of  $0.2 \text{ A g}^{-1}$ . After 200 cycles, the specific discharge capacities of NF-P 400, NF-P 500 and NF-P 800 electrodes are 237.5, 431.1 and  $268.5 \text{ mAh g}^{-1}$ , with corresponding capacity retention rate of 28.8 %, 53.5 % and 49.4 %, respectively. Among these three materials, the mass percentage of C for NF-P 500 is 63.4 %, which is the main reason causes the low capacity. Meanwhile, the content of  $\text{NiFe}_2\text{O}_4$  for NF-P 500 (8.1 wt%) is less than NF-P 400 (32.7 wt%), but its specific capacity is higher than that of NF-P 400 after 200 cycles at  $0.2 \text{ A g}^{-1}$  and the NF-P 500 shows the best capacity retention rate. Table 1 summarizes the capacities of the three anode materials, showing that the NF-P 800 has a better cycling stability than NF-P 500. In this context, the excellent cycling and rate performances of NF-P 500 are mainly attributed to the following reasons: i) the carbon fibers can effectively alleviate volume expansion and structural stress during cycling process; ii)  $\text{Fe}_{0.64}\text{Ni}_{0.36}$  alloy can inhibit the generation of lithium dendrites and effectively reduce the nucleation overpotential of metallic lithium, thereby improving its electrochemical stability [9]; iii) the heterostructure can improve electrochemical properties through a



**Fig. 3.** XRD patterns of (a) NF-P 800, (b) NF-P 500 and (c) NF-P 400. Full XPS spectra of (d) NF-P 400 and (g) NF-P 800. XPS spectra of Ni 2p (e) and Fe 2p (f) for NF-P 400. XPS spectra of Ni 2p (h) and Fe 2p (i) and for NF-P 800.



**Fig. 4.** (a) CV of the third cycle at a scan rate of 0.1 mV s<sup>-1</sup>. (b) Initial voltage versus capacity curves at a current density of 0.2 A g<sup>-1</sup> for NF-P 400, NF-P 500 and NF-P 800. (c) Rate performance at different current densities. (d) Cycling performance at a current density 0.2 A g<sup>-1</sup>.

**Table 1**

Summary of specific capacities for different anode materials.

Anode materials	Initial discharge capacity (mAh g <sup>-1</sup> )	Capacity after 200 cycles at 0.2 A g <sup>-1</sup> (mAh g <sup>-1</sup> )	Capacity retention rate
NiFe <sub>2</sub> O <sub>4</sub> @CNFs	826	237.5	28.5 %
NiFe <sub>2</sub> O <sub>4</sub> /Fe <sub>0.64</sub> Ni <sub>0.36</sub> @CNFs	806	431.1	53.5 %
Fe <sub>0.64</sub> Ni <sub>0.36</sub> @CNFs	543	268.5	49.4 %

synergistic interaction between NiFe<sub>2</sub>O<sub>4</sub> and Fe<sub>0.64</sub>Ni<sub>0.36</sub>. The catalytic Fe<sub>0.64</sub>Ni<sub>0.36</sub> not only facilitate the conversion reaction of NiFe<sub>2</sub>O<sub>4</sub>, resulting in the high capacity, but also increase the conductivity of the material [24,25].

To further elucidate the excellent electrochemical performance of heterostructured NiFe<sub>2</sub>O<sub>4</sub>/Fe<sub>0.64</sub>Ni<sub>0.36</sub> electrode, a series of CV tests on pure-phase (NiFe<sub>2</sub>O<sub>4</sub> and Fe<sub>0.64</sub>Ni<sub>0.36</sub>) electrodes are performed. From Fig. 5a, it can be seen that the CV curves of NiFe<sub>2</sub>O<sub>4</sub> electrode have similar profiles at different scan rates, indicating that similar electrochemical reactions take place during cycling. The relationship between

the current (*i*) and scan rate (*v*) are studied by the power-law equation [26].

$$i = av^b \quad (4)$$

Where *a* and *b* are constants, and the value of *b* is determined by the slope of log(*i*) against log(*v*) [27]. Typically, when *b* value is 0.5 and 1.0, the lithium storage is mainly governed by diffusion-controlled and pseudocapacitive process, respectively [28,29]. For the NiFe<sub>2</sub>O<sub>4</sub> electrode, Fig. 5b shows the *b* values are close to 0.5 for both cathodic peak (0.59) and anodic peak (0.74), indicating that the lithium storage behavior is dominated by diffusion-controlled process. Furthermore, the contribution rates of diffusion-controlled and pseudocapacitive processes at different scan rates can be further quantified by Eq. (5) [27]:

$$i = k_1v + k_2v^{1/2} \quad (5)$$

Where *k*<sub>1</sub>*v* and *k*<sub>2</sub>*v*<sup>1/2</sup> represent the contributions of diffusion-controlled and pseudocapacitive, respectively. For NiFe<sub>2</sub>O<sub>4</sub>, the pseudocapacitive proportion at 0.5 mV s<sup>-1</sup> is described in Fig. 5c, showing a low contribution rate (blue region) of 4 % to the total capacity. In Fig. 5d, the contribution rates of diffusion-controlled process are 98 %, 97 %, 96 %, 94 % and 93 % at the scan rates of 0.1, 0.3, 0.5, 0.8 and 1.0 mV s<sup>-1</sup>, respectively. In this context, the lithium storage behavior of

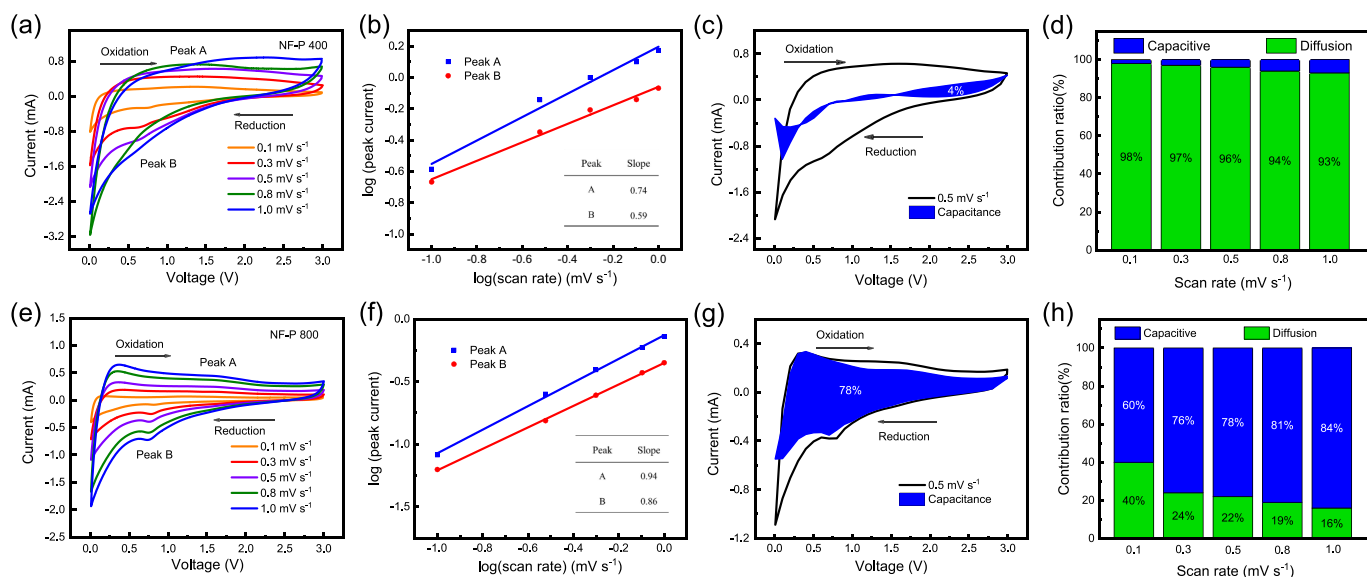


**Fig. 5.** CV curves of NF-P 400 (a) and NF-P 800 (e); Values of  $b$  (slope) for NF-P 400 (b) and NF-P 800 (f); Contribution rate of capacitance at  $0.5 \text{ mV s}^{-1}$  for NF-P 400 (c) and NF-P 800 (g); Diffusion-controlled (green region) and pseudocapacitance (blue region) contribution at various scan rates for NF-P 400 (d) and NF-P 800 (h). (For interpretation of the references to colour in this figure legend, the reader is referred to the web version of this article.)

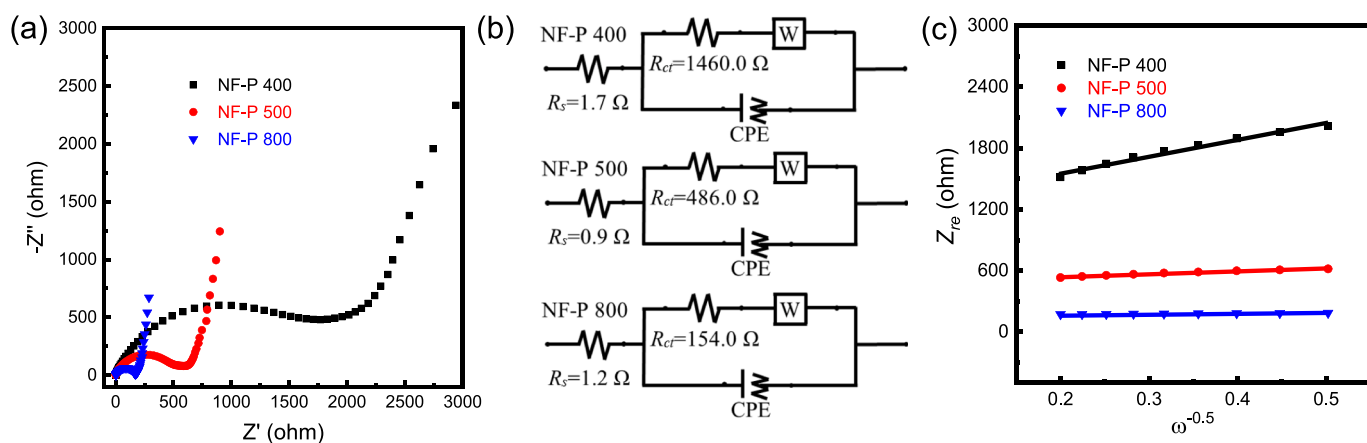


**Fig. 6.** (a) EIS spectra of NF-P membrane electrodes. (b) Equivalent circuit diagrams. (c) Graph of  $Z_{re}$  plotted against  $\omega^{-0.5}$ .

**Table 2**

The  $\sigma$  and  $D_{Li}$  of different anode materials.

Anode materials	$\sigma$ ( $\Omega \text{ s}^{-0.5}$ )	$D_{Li}$ ( $\text{cm}^2 \text{ s}^{-1}$ )
$\text{NiFe}_2\text{O}_4$ @CNFs	1641.2	$2.6 \times 10^{-27}$
$\text{NiFe}_2\text{O}_4/\text{Fe}_{0.64}\text{Ni}_{0.36}$ @CNFs	257.6	$8.7 \times 10^{-26}$
$\text{Fe}_{0.64}\text{Ni}_{0.36}$ @CNFs	56.1	$1.1 \times 10^{-23}$

$\text{NiFe}_2\text{O}_4$  is mainly governed by diffusion-controlled process at the scan rate of  $0.1\text{--}1.0 \text{ mV s}^{-1}$ . As mentioned herebefore, the lithium storage mechanism of  $\text{NiFe}_2\text{O}_4$  electrode is intercalation-conversion reaction, which is affected by the diffusion rate of  $\text{Li}^+$  [30]. For the NF-P 800 electrode, Fig. 5e shows that the CV curves also display similar profiles at scan rates of from  $0.1$  to  $1.0 \text{ mV s}^{-1}$ . Meanwhile, Fig. 5f manifests the  $b$  values of cathodic peak (0.86) and anodic peak (0.94) are close to 1.0, which means that the lithium-ion storage behavior is dominated by a pseudocapacitive process. Furthermore, it can be seen from Fig. 5g that 78% of lithium storage is calculated as pseudocapacitance (blue region) at the scan rate of  $0.3 \text{ mV s}^{-1}$ . Finally, Fig. 5h shows that the contribution rates of diffusion-controlled and pseudocapacitive processes for NF-P

800 electrode at scan rates from  $0.1$  to  $1.0 \text{ mV s}^{-1}$ , indicating that the lithium storage behavior of  $\text{Fe}_{0.64}\text{Ni}_{0.36}$  electrode is mainly governed by a pseudocapacitive process. The storage mechanism of lithium ions is changed from intercalation for  $\text{NiFe}_2\text{O}_4$  to surface reaction for  $\text{Fe}_{0.64}\text{Ni}_{0.36}$ , which can be attributed to the increase of the  $\text{Fe}_{0.64}\text{Ni}_{0.36}$  content and the diameter reduction of the CNFs with increasing annealing temperature, leading to better cycling performance [9,29]. For  $\text{NiFe}_2\text{O}_4$ , the lithium storage behavior is mainly governed by diffusion-controlled process, which is conducive to the specific capacity of anodes; for  $\text{Fe}_{0.64}\text{Ni}_{0.36}$ , the lithium storage behavior is dominated by a pseudocapacitive process, which is beneficial to the cycling performance of anodes. This can prove that the high specific capacity, excellent cycling stability and rate performances of  $\text{NiFe}_2\text{O}_4/\text{Fe}_{0.64}\text{Ni}_{0.36}$  results from the synergistic interaction between different components in the heterostructure.

EIS spectra are performed to further investigate the electrochemical reaction kinetics of NF-P 400, NF-P 500 and NF-P 800 electrodes (Fig. 6a). It can be seen that all the spectra consist of a semicircle in the high-frequency region and an inclined line in the low-frequency region. Moreover, these EIS spectra can be fitted with equivalent circuit

**Table 3**  
Electrochemical performance comparison of NiFe<sub>2</sub>O<sub>4</sub> composite anodes for LIBs.

Anode materials	Cycling performance			Rate capability		Ref.
	Current density (A g <sup>-1</sup> )	Cycle number	Capacity (mAh g <sup>-1</sup> )	Current density (A g <sup>-1</sup> )	Capacity (mAh g <sup>-1</sup> )	
Spherical NiFe <sub>2</sub> O <sub>4</sub> /graphene	0.1	50	407	0.3 0.6	489 353	[36]
NiFe <sub>2</sub> O <sub>4</sub> composite	0.1	100	223	0.2 0.5	< 200 < 200	[37]
NiFe <sub>2</sub> O <sub>4</sub> prepared with Na <sub>2</sub> CO <sub>3</sub>	0.1	100	438.6	0.4 1.0	401.7 351.8	[38]
NiFe <sub>2</sub> O <sub>4</sub> @CNFs	1.0	60	411	0.2 0.5	670 542	[39]
NiFe <sub>2</sub> O <sub>4</sub> /C nanofibers	0.1	100	497	0.5 1.0	304 228	[8]
NiFe <sub>2</sub> O <sub>4</sub> /Fe <sub>0.64</sub> Ni <sub>0.36</sub> @CNFs	0.2	200	431.1	0.1 1.0	558.5 272.4	This work

diagrams in Fig. 6b, where  $R_s$ ,  $R_{ct}$ ,  $W$  and CPE represent electrolyte resistance, charge transfer resistance, Warburg impedance and double-layer capacitance, respectively [30,31]. In addition, the semicircle diameters of the NF-P 400, NF-P 500 and NF-P 800 electrodes gradually decrease in the high frequency region, indicating that the as-prepared electrodes obtained at higher annealing temperatures have lower charge transfer impedance. Meanwhile, the inclined line in the low-frequency region is associated with lithium-ion diffusion in the electrode. The diffusion coefficient of lithium ion ( $D_{Li}$ ) can be calculated by Eqs. (6) and (7) [32,33].

$$D_{Li} = \frac{R^2 T^2}{2A^2 n^4 F^4 C^2 \sigma^2} \quad (6)$$

$$Z' = R_s + R_{ct} + \sigma \omega^{-0.5} \quad (7)$$

The parameters in the two equations are as follows:  $F$  (Faraday constant) = 96,485C mol<sup>-1</sup>,  $R$  (gas constant) = 8.314 J k<sup>-1</sup> mol<sup>-1</sup>,  $A$  (electrode area) =  $1.54 \times 10^{-4}$  m<sup>2</sup>,  $T$  = 298.15 K,  $n$  is the number of transferred electrons during conversion of per single molecule (*i.e.*, NiFe<sub>2</sub>O<sub>4</sub>,  $n$  = 8) and  $C$  is the concentration of lithium ions. Fig. 6c show the graph of  $Z_{re}$  plotted against  $\omega^{-0.5}$ . The  $\sigma$  value of the NF-P 400, NF-P 500 and NF-P 800 electrodes is 1641.2, 257.6 and 56.1  $\Omega$  s<sup>-0.5</sup>, respectively. The  $D_{Li}$  of NF-P 400, NF-P 500 and NF-P 800 electrodes is calculated to be  $2.6 \times 10^{-27}$ ,  $8.7 \times 10^{-26}$  and  $1.1 \times 10^{-23}$  cm<sup>2</sup> s<sup>-1</sup>, respectively (Table 2). In addition, the impedance spectrum and  $Z_{re}$  vs  $\omega^{-0.5}$  curve of pure CNF was shown in Fig. S3, where P 800 represents pure CNF. It can be seen that the  $D_{Li}$  gradually increases with the increase of annealing temperature, which is related to the diffusion path of lithium ions and the pseudocapacitive behavior [34]. On the one hand, with the increase of annealing temperature, the diameter of fibers decreases gradually, resulting in the short diffusion path for lithium ions. On the other hand, the content of Fe<sub>0.64</sub>Ni<sub>0.36</sub> increases significantly in the fibers with the increase of annealing temperature, which can inhibit the generation of lithium dendrites and effectively reduce the nucleation overpotential of metallic lithium [35]. It can be deduced for the anode materials that the higher annealing temperature, the lower charge-transfer impedance and better lithium-ion diffusion ability. Table 3 summarizes the electrochemical performance of NiFe<sub>2</sub>O<sub>4</sub> composite anodes for LIBs in the previous literature.

#### 4. Conclusions

Ni-Fe based nanoparticles emdedded in CNFs are prepared by electrospinning followed by subsequent annealing, and used as anode materials for LIBs. Three distinct Ni-Fe based nanoparticles are obtained, including NiFe<sub>2</sub>O<sub>4</sub> (400 °C), heterostructured NiFe<sub>2</sub>O<sub>4</sub>/Fe<sub>0.64</sub>Ni<sub>0.36</sub> (500 °C) and Fe<sub>0.64</sub>Ni<sub>0.36</sub> (800 °C). When used as anode materials, NF-P 500 exhibits a specific discharge capacity of 431.1 mAh

g<sup>-1</sup> after 200 cycles at a current density of 0.2 A g<sup>-1</sup>, higher than that of NiFe<sub>2</sub>O<sub>4</sub>@CNFs (237.5 mAh g<sup>-1</sup>) and Fe<sub>0.64</sub>Ni<sub>0.36</sub>@CNFs (268.5 mAh g<sup>-1</sup>) electrodes. As the annealing temperature increases, the diameter of the CNFs gradually shrinks, which is beneficial to the cycling stability of LIBs due to the shortened diffusion path for Li ions. The increasing content of Fe<sub>0.64</sub>Ni<sub>0.36</sub> in the fiber membranes can improve the contribution rates of pseudocapacitive process. Moreover, the synergistic effect of heterostructured NiFe<sub>2</sub>O<sub>4</sub>/Fe<sub>0.64</sub>Ni<sub>0.36</sub> can further improve the electrochemical performance. The catalytic Fe<sub>0.64</sub>Ni<sub>0.36</sub> not only facilitate the conversion reaction of NiFe<sub>2</sub>O<sub>4</sub>, resulting in the high capacity, but also increase the conductivity of the material. This work provides a feasible strategy to prepare heterostructured bimetallic compounds embedded in CNFs as anode materials, paving the road for the development of high-performance LIBs.

#### CRediT authorship contribution statement

**Shujin Hao:** Formal analysis, Investigation, Writing – original draft. **Xiaoli Sheng:** Formal analysis, Investigation. **Fei Xie:** Formal analysis, Writing – review & editing. **Meng Sun:** Formal analysis, Validation. **Feiyu Diao:** Formal analysis, Methodology, Writing – review & editing. **Yiqian Wang:** Conceptualization, Funding acquisition, Supervision, Writing – review & editing.

#### Declaration of competing interest

There are no conflicts to declare.

#### Data availability

Data will be made available on request.

#### Acknowledgments

The authors express their gratitude for the financial support received from various sources, including the High-end Foreign Experts Recruitment Programs (Grant Nos.: GDW20173500154, GDW20163500110), the Shandong Province “Double-Hundred Talent Plan” (Grant No.: WST2018006), the Shandong Province High-end Foreign Experts Recruitment Program, and the Top-notch Innovative Talent Program of Qingdao City, China (Grant no.: 13-CX-8). Thanks for helpful discussion with Professor Francois Schiettekatte from University of Montréal, Canada. Y. Q. Wang would like to acknowledge the support received from the Taishan Scholar Program of Shandong Province, China, the Qingdao International Center of Semiconductor Photoelectric Nanomaterials, and the Shandong Provincial University Key Laboratory of Photoelectrical Material Physics and Devices.

## Appendix A. Supplementary data

Supplementary data to this article can be found online at <https://doi.org/10.1016/j.est.2023.110412>.

## References

- [1] H. Yu, H. Fan, B. Yadian, H. Tan, W. Liu, H.H. Hng, Y. Huang, Q. Yan, General approach for MOF-derived porous spinel  $\text{AFe}_2\text{O}_4$  hollow structures and their superior lithium storage properties, *ACS Appl. Mater. Interfaces* 7 (2015) 26751–26757.
- [2] M. Li, Y. Xiong, X. Liu, X. Bo, Y. Zhang, C. Han, L. Guo, Facile synthesis of electrospun  $\text{MFe}_2\text{O}_4$  ( $\text{M} = \text{Co}, \text{Ni}, \text{Cu}, \text{Mn}$ ) spinel nanofibers with excellent electrocatalytic properties for oxygen evolution and hydrogen peroxide reduction, *Nanoscale* 7 (2015) 8920–8930.
- [3] G. Liu, J. Wang, X. Sheng, X. Xue, Y. Wang, Thermodynamics and electronic structure characteristics of  $\text{MFe}_2\text{O}_4$  with different spinel structures: a first-principles study, *Ceram. Int.* 49 (2023) 29747–29754.
- [4] Y. Zhao, X. Li, B. Yan, D. Xiong, D. Li, S. Lawes, X. Sun, Recent developments and understanding of novel mixed transition-metal oxides as anodes in lithium ion batteries, *Adv. Energy Mater.* 6 (2016) 1502175.
- [5] K. Cao, T. Jin, L. Yang, L. Jiao, Recent progress in conversion reason mental oxide anodes for Li-ion batteries, *Mater. Chem. Front.* 1 (2017) 2213–2242.
- [6] X. Sheng, T. Li, M. Sun, G. Liu, Q. Zhang, Z. Ling, S. Gao, F. Diao, J. Zhang, F. Rosei, Y.Q. Wang, Flexible electrospun iron compounds/carbon fibers: phase transformation and electrochemical properties, *Electrochim. Acta* 407 (2022) 139892.
- [7] P. Santhoshkumar, S.H. Kang, N. Shaji, C.W. Lee, Incorporation of binary metal oxide and one dimensional carbon fiber hybrid nanocomposites for electrochemical energy storage applications, *J. Alloys Compd.* 842 (2020) 155649.
- [8] T. Dong, G. Wang, P. Yang, Electrospun  $\text{NiFe}_2\text{O}_4/\text{C}$  fibers as high-performance anodes for lithium-ion batteries, *Diam. Relat. Mater.* 73 (2017) 210–217.
- [9] Z. Yu, J. Zhou, X. Lv, C. Li, X. Liu, S. Yang, Y. Liu, Nitrogen-doped porous carbon nanofiber decorated with FeNi alloy for dendrite-free high-performance lithium metal anode, *J. Alloys Compd.* 925 (2022) 166691.
- [10] S. Yuan, Q. Lai, X. Duan, Q. Wang, Carbon-based materials as anode materials for lithium-ion batteries and lithium-ion capacitors: a review, *J Energy Storage* 61 (2023) 106716.
- [11] H. Fu, Q. Wen, P. Li, Z. Wang, Z. He, C. Yan, J. Mao, K. Dai, X. Zhang, J. Zheng, Recent advances on heterojunction-type anode materials for lithium-/sodium-ion batteries, *Small Methods* 6 (2022) 2201025.
- [12] Z. Cui, M. Sun, H. Liu, S. Li, Q. Zhang, C. Yang, G. Liu, J. Zhong, Double-shell  $\text{SnO}_2/\text{Fe}_2\text{O}_3$  hollow spheres as a high-performance anode materials for lithium-ion batteries, *CrystEngComm* 22 (2020) 1197–1208.
- [13] Y. Wang, S. Wu, C. Wang, Y. Wang, X. Han, Morphology controllable synthesis of  $\text{NiO}/\text{NiFe}_2\text{O}_4$  hetero-structures for ultrafast lithium-ion battery, *Front. Chem.* 6 (2019) 654.
- [14] J. Wang, X. Sheng, S. Hao, G. Liu, R. Cai, X. Xue, Y. Wang, Construction of  $\text{Fe}_{0.64}\text{Ni}_{0.36}$ @graphite nanoparticles via corrosion-like transformation from  $\text{NiFe}_2\text{O}_4$  and surface graphitization in flexible carbon nanofibers to achieve strong wideband microwave absorption, *J. Colloid Interface Sci.* 657 (2024) 193–207.
- [15] M. Fu, Q. Jiao, Y. Zhao, Preparation of  $\text{NiFe}_2\text{O}_4$  nanorod-graphene composites via an ionic liquid assisted one-step hydrothermal approach and their microwave absorbing properties, *J. Mater. Chem. A* 1 (2013) 5577–5586.
- [16] Z. Yu, T. Lin, C. Zhu, J. Li, X. Luo, Design of trimetallic  $\text{NiMoFe}$  hollow microspheres with polyoxometalate-based metal-organic frameworks for enhanced oxygen evolution reaction, *ChemElectroChem* 8 (2021) 1316–1321.
- [17] R.S. Yadav, I. Kuritka, J. Vilcakova, J. Havlica, J. Masilko, L. Kalina, J. Tkacz, V. Enev, M. Hajdúchová, Structural, magnetic, dielectric, and electrical properties of  $\text{NiFe}_2\text{O}_4$  spinel ferrite nanoparticles prepared by honey-mediated sol-gel combustion, *J. Phys. Chem. Solids* 107 (2017) 150–161.
- [18] H. Chen, L. Zhou, M. Wen, Q. Wu, C. Wang, A branched-dumbbell  $\text{Pt}/\text{NiFe}$  nanostructure and its high catalytic reduction activity for nitro-aromatic compounds, *Mater. Res. Bull.* 60 (2014) 322–327.
- [19] J.J. Wang, X.Y. Xue, Y.Q. Wang, Tuning the structural and magnetic properties of electrospun strontium-iron-oxide nanofibers with different stoichiometry, *Mater. Charact.* 200 (2023) 112884.
- [20] Y. Xiao, J. Zai, B. Tian, X. Qian, Formation of  $\text{NiFe}_2\text{O}_4$ /expanded graphite nanocomposites with superior lithium storage properties, *Nano-Micro Lett.* 9 (2017) 34.
- [21] Y. Fu, Y. Wan, H. Xia, X. Wang, Nickel ferrite-graphene heteroarchitectures: toward high-performance anode materials for lithium-ion batteries, *J. Power Sources* 213 (2012) 338–342.
- [22] B. Xu, L. Yu, X. Zhao, H. Wang, C. Wang, L. Zhang, G. Wu, Simple and effective synthesis of zinc ferrite nanoparticle immobilized by reduced graphene oxide as anode for lithium-ion batteries, *J. Colloid Interface Sci.* 584 (2021) 827–837.
- [23] C. Yang, C. Peng, P. Chen, C. Ma, K. Guo, Y. Cheng, Insights into electrochemical performances of  $\text{NiFe}_2\text{O}_4$  for lithium-ion anode materials, *J. Alloys Compd.* 896 (2022) 163079.
- [24] T. Xin, F. Diao, C. Li, H. Feng, G. Liu, J. Zou, Y. Ding, B. Liu, Y. Wang, Synergistic effect of hierarchical  $\text{SnO}_2$  nanorods/ $\text{Fe}_2\text{O}_3$  hexahedrons with enhanced performance as lithium ion battery anodes, *Mater. Res. Bull.* 99 (2018) 196–203.
- [25] G. Xiao, W. Cai, L. Zhu, Y. Fang, H. Ao, Y. Zhu, Y. Qian, N-Doped carbon nanotubes decorated with Fe/Ni sites to stabilize lithium metal anodes, *Inorg. Chem. Front.* 7 (2020) 2747–2752.
- [26] M. Vincent, V.S. Avvaru, M. Haranczyk, V. Etacheri, Fast-charging and long-lasting Mg-Na hybrid batteries based on extremely pseudocapacitive bronze  $\text{TiO}_2$  nanosheet cathodes, *Chem. Eng. J.* 433 (2022) 133810.
- [27] A.Y. Shenouda, H. Liu, Electrochemical behaviour of tin borophosphate negative electrodes for energy storage systems, *J. Power Sources* 185 (2008) 1386–1391.
- [28] M. Vincent, S.S. Kumar, D. Kowalski, Pseudocapacitive vs diffusion controlled charge storage in  $\text{Fe}_2\text{O}_3$  nanosheet Na-ion battery, *Electrochim. Acta* 469 (2023) 143161.
- [29] Y. Tang, L. Liu, H. Zhao, Y. Zhang, L. Kong, S. Gao, X. Li, L. Wang, D. Jia, Pseudocapacitive behaviors of  $\text{Li}_2\text{FeTiO}_4/\text{C}$  hybrid porous nanotubes for novel lithium-ion battery anodes with superior performances, *ACS Appl. Mater. Interfaces* 10 (2018) 20225–20230.
- [30] F. Li, Y. Li, L. Zhao, J. Liu, F. Zuo, F. Gu, H. Liu, R. Liu, Y. Li, J. Zhan, Q. Li, H. Li, Revealing an intercalation-conversion-heterogeneity hybrid lithium-ion storage mechanism in transition metal nitrides electrodes with jointly fast charging capability and high energy output, *Adv. Sci.* 9 (2022) 2203895.
- [31] F. Xie, X. Sheng, Z. Ling, S. Hao, Q. Zhang, M. Sun, G. Liu, F. Diao, Y.Q. Wang, Flexible electrospun iron/manganese-based compounds/carbon fibers: phase transformation and electrochemical properties, *Electrochim. Acta* 470 (2023) 143288.
- [32] W. Zhang, X. Wu, J. Hu, Y. Guo, L. Wan, Carbon coated  $\text{Fe}_3\text{O}_4$  nanospindles as a superior anode materials for lithium-ion batteries, *Adv. Funct. Mater.* 18 (2008) 3941–3946.
- [33] M. Sun, Z. Cui, H. Liu, S. Li, Q. Zhang, X. Sheng, Y.Q. Wang, Graphene-wrapped  $\text{FeOOH}$  nanorods with enhanced performance as lithium-ion battery anode, *NANO* 16 (2021) 2150005.
- [34] X. Li, Y. Zhang, S. Wang, Y. Liu, Y. Ding, G. He, X. Jiang, W. Xiao, G. Yu, Scalable high-areal-capacity Li-S batteries enabled by sandwich-structured hierarchically porous membranes with intrinsic polysulfide adsorption, *Nano Lett.* 20 (2020) 6922–6929.
- [35] Y. Xin, S. Nie, S. Pan, C. Miao, H. Mou, M. Wen, W. Xiao, Electrospinning fabrication of  $\text{Sb-SnSb}/\text{TiO}_2/\text{CNFs}$  composite nanofibers as high-performance anodes for lithium-ion batteries, *J. Colloid Interface Sci.* 630 (2023) 403–414.
- [36] X. Chen, Y. Huang, K. Zhang, X. Feng, S. Li, Self-assembled flower-like  $\text{NiFe}_2\text{O}_4$  decorated on 2D graphene nanosheets composite and their excellent electrochemical performance as anode materials for LIBs, *J. Alloys Compd.* 686 (2016) 905–913.
- [37] Y. Zou, Z. Li, Y. Liu, J. Duan, B. Long, Coaxial structure of  $\text{NiFe}_2\text{O}_4/\text{CNTs}$  composites as anodes for enhanced lithium ion batteries, *J. Alloys Compd.* 820 (2020) 153085.
- [38] S. Dai, X. Tang, X. Li, J. Zhang, Z. Shao, Synthesis of  $\text{NiFe}_2\text{O}_4$  with different precipitation agents for Li-ion battery anode material by co-precipitation, *J. Solid State Electrochem.* 26 (2022) 1211–1220.
- [39] L. Lou, R. Cui, K. Liu, H. Qiao, Q. Wei, Electrospun preparation and lithium storage properties of  $\text{NiFe}_2\text{O}_4$  nanofibers, *Ionics* 21 (2015) 687–694.